



## 1. INTRODUCTION

Planetary magnetospheres are continuously immersed in the solar wind, which influences their global morphology and drives dynamics through energy transfer (Russell 2001). Distinguishing and monitoring magnetospheric states, whether strongly compressed by the solar wind or expanded under quiet conditions, is crucial for advancing our understanding of dynamic magnetospheric processes beyond static equilibrium descriptions. Among the planets in the solar system, Jupiter has the strongest magnetic field and the largest magnetosphere (e.g., Bagenal 2007), making it a unique laboratory for investigating solar wind-magnetosphere interactions at extreme scales and yielding insights into fundamental magnetospheric physics.

However, unlike Earth with spacecraft positioned at the L1 point that can continuously monitor in situ solar wind parameters, Jupiter and other planets lack such upstream measurements for real-time determination of magnetospheric states. Solar wind conditions at outer planets are typically estimated by extrapolating Earth-based measurements using propagation models (Barnard & Owens 2022; Keebler et al. 2022; Odstrcil 2003; Owens et al. 2020; Rutala et al. 2024; Tao et al. 2005; Zieger & Hansen 2008). While these models provide valuable quantitative estimates, they are nevertheless constrained by the complexity of solar wind evolution. For Jupiter specifically, model validations against in situ measurements have revealed timing uncertainties reaching  $\pm 4$  days (Jian et al. 2015; Keebler et al. 2022; Reiss et al. 2023; Rutala et al. 2024; Tao et al. 2005; Zieger & Hansen 2008). This level of uncertainty is a crucial limit to our understanding of Jupiter's magnetospheric dynamics that often exhibit significant changes on smaller timescales (Gurnett et al. 2002; Krupp et al. 2004; Nichols et al. 2017), hindering temporal correlation studies and the identification of response mechanisms.

Potentially, these challenges could be partially addressed through in situ observations. Spacecraft at Jupiter can capture solar wind parameters outside the magnetosphere (e.g., Ebert et al. 2014; McComas et al. 2017), or acquire magnetopause standoff distances during boundary crossings (e.g., Bame et al. 1992; Bridge et al. 1979a; Bridge et al. 1979b; Smith et al. 1978). However, such direct measurements also have limitations: acquiring upstream conditions typically sacrifices contemporaneous magnetospheric monitoring, and spacecraft spend the majority of their

64 operational time inside the magnetosphere, where direct measurement of  
65 solar wind parameters is not feasible.

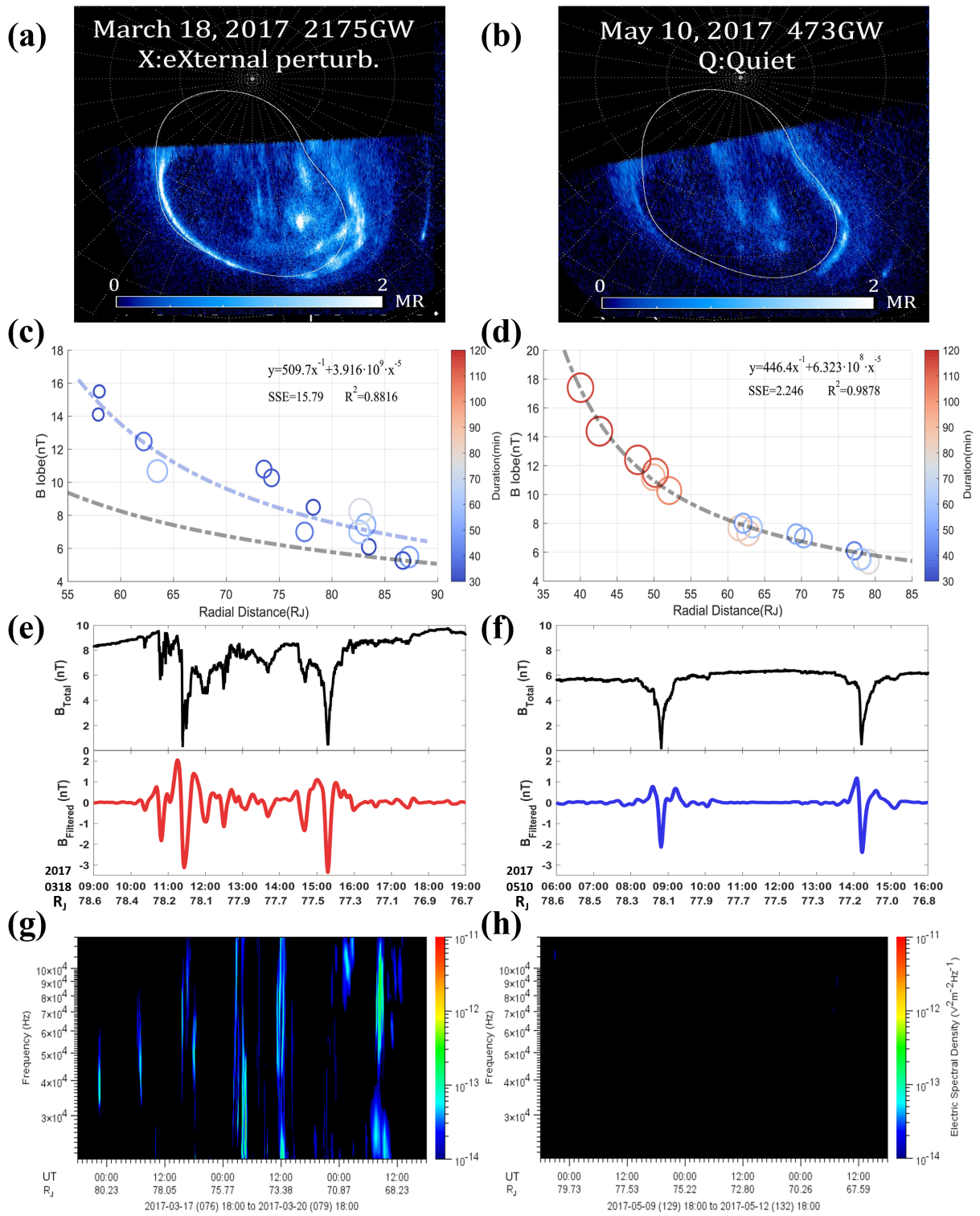
66 To enable continuous magnetospheric state examination, robust correlations  
67 between external solar wind conditions and internal magnetospheric  
68 responses would be highly valuable. Once validated, these correlations  
69 allow us to identify magnetospheric states using continuously observable  
70 proxies, facilitating further studies on solar wind-magnetosphere  
71 interactions even without direct upstream measurements and temporally  
72 accurate model output. Establishing these correlations critically depends  
73 on coordinated observations to separate spatial and temporal effects. Key  
74 opportunities include: (1) Multi-spacecraft conjunctions (e.g., the  
75 Cassini-Galileo overlap period; Krupp et al. 2002; Kurth et al. 2002)  
76 enabling simultaneous solar wind and magnetospheric measurements, and (2)  
77 synergistic use of remote sensing data (e.g., auroral emissions monitored  
78 by telescopes and spacecrafts) alongside in situ measurements of solar  
79 wind (e.g., Nichols et al. 2007, 2017) or magnetospheric phenomena (e.g.,  
80 Yao et al. 2022). These joint datasets have been leveraged in previous  
81 studies to establish linkages between upstream solar wind conditions and  
82 various magnetospheric responses, including auroras, magnetic fields, ULF  
83 waves, and radio emissions (as will be detailed in Section 2).

84 In this study, we consolidate these diverse observational signatures to  
85 reveal that Jupiter's magnetosphere exhibits two distinct states  
86 ("compressed" and "quiet") under varying solar wind forcing. We further  
87 develop and present practical identification criteria using available in  
88 situ and remote sensing measurements, and verify their effectiveness via  
89 cross-validation using Juno's measurements.

## 90 2. POTENTIAL PROXIES FOR JOVIAN MAGNETOSPHERIC STATES

91 In this section, we evaluate four potential proxies for Jovian  
92 magnetospheric states, reviewing their documented responses to varying  
93 external conditions. We develop an identification framework for each  
94 proxy, based on its observational characteristics and distributions,  
95 detailing specific criteria, valid ranges of applicability, and practical  
96 considerations. The analysis primarily utilizes data from the Juno  
97 spacecraft, which carries the MAG instrument for magnetic field  
98 measurements (Connerney et al. 2017) and the Waves instrument for  
99 observing radio emissions (Kurth et al. 2017). Applying the classification  
100 methods to a comprehensive dataset spanning from July 7, 2016 to July 7,  
101

2023, we generate time catalogs of both quiet and compressed states for further analysis.



105 Figure 1. Comparisons of magnetospheric phenomena between compressed and  
106 quiet states. Two representative UV auroral images for the (a) X-family  
107 aurora and (b) Q-family aurora identified by Grodent et al. (2018). Each  
108 image is labeled with the observation date, total power, and auroral  
109 morphology. The magnetic field in lobe-like region,  $B_{lobe-like}$ , across  
110 different radial distances in (c) the compressed (blue) and (d) the quiet  
111 (gray) magnetosphere (from Xu et al. 2023). Each circle's colour and size  
112 in (c, d) represent the duration of the spacecraft crossing the current  
113 sheet, a proxy for the current sheet thickness. Total magnetic field  
114 strengths and magnetic field fluctuations using a 4th-order Butterworth  
115 filter to produce 10-60 minute bandpass-filtered results of (e) the  
116 compressed magnetosphere, which shows significant fluctuations and (f) the  
117 quiet magnetosphere where almost no magnetic field fluctuations appear  
118 (modified from Sun et al. 2024). Measurements of radio emissions in (g)  
119 the compressed magnetosphere, showing prominent broadband kilometric  
120 (bKOM) emission features and (h) quiet magnetosphere where almost no bKOM  
121 radio emissions are detected (modified from Chen et al. 2024). These  
122 phenomena present concurrent responses to changes in the magnetospheric  
123 states.

124

## 125 2.1. Auroras

126 Auroral emissions serve as a direct proxy of energy dissipation in the  
127 magnetosphere (Bonfond et al. 2021; Yao et al. 2019). Coordinated datasets  
128 of in situ measurements and remote auroral imaging provide an  
129 unprecedented opportunity to connect auroral morphologies to upstream  
130 drivers. Gurnett et al. (2002) presented a seminal case with simultaneous  
131 observations, in which Cassini and Galileo sequentially captured  
132 interplanetary shock signals near Jupiter, followed by a peak in auroral  
133 intensities detected by Cassini's UV spectrograph. Similarly, Nichols et  
134 al. (2007, 2017) combined in situ interplanetary measurements with HST  
135 auroral observations, revealing that the brightness of Jupiter's main  
136 emissions significantly increased during enhanced solar wind conditions  
137 compared to quiet intervals. Furthermore, Yao et al. (2022) conducted a  
138 comprehensive statistical analysis, demonstrating that all compression  
139 events associated with reduced magnetopause standoff distances coincided  
140 with main auroral brightening (MAB) morphologies, with no instances of dim  
141 auroral emissions. Subsequent studies by Head et al. (2024, 2025) further  
142 elucidated that magnetospheric compression could trigger a global

143 contraction of the main emissions, along with the appearance of auroral  
144 bridges. These results collectively confirm that Jupiter's auroral  
145 morphology, particularly the main emissions, indeed exhibits significant  
146 modulation under different solar wind conditions.

147 The classification framework proposed by Grodent et al. (2018)  
148 discriminates between different auroral morphologies and categorizes them  
149 into six families. Among them, the X-family auroras (consistent with the  
150 definition of MAB events; see Figure 1(a)) display a bright, narrow, and  
151 sharply defined band on the dawnside, often accompanied by dynamic  
152 structures in the dusk sector. In contrast, the Q-family auroras (Figure  
153 1(b)) exhibit extremely low emission power, with the main emissions often  
154 barely distinguishable. Based on the studies discussed above, the Q-family  
155 auroras are believed to correspond to a quiet and undisturbed  
156 magnetosphere, while the X-family auroras indicate significant  
157 magnetospheric compression. Grodent et al. (2018) and Palmaerts et al.  
158 (2024) systematically labelled auroral images obtained from the HST  
159 programs GO-14634 and GO-15638, respectively. From their lists, we obtain  
160 a total of 19 quiet (Q-family) and 14 compressed (X-family) magnetospheric  
161 events. While morphological classification involves inherent subjectivity,  
162 this aurora-derived dataset provides a valuable benchmark: unlike single-  
163 point measurements, auroral imaging captures the global magnetospheric  
164 state instantaneously. And its reliability is anchored in  
165 correlations directly established through unambiguous, simultaneous  
166 observations of auroral morphologies and solar wind conditions.

## 167 2.2. Statistical Distribution of Lobe-like Magnetic Fields

168 Due to the tilt between Jupiter's magnetic dipole and its rotation axis,  
169 the current sheet oscillates with a period of approximately 10 hours.  
170 Consequently, spacecraft periodically enter the current sheet and exit  
171 into regions characterized by relatively stable magnetic field strengths  
172 and low plasma density as shown in Figure 2(a) and 2(b). While sharing  
173 similarities with the terrestrial magnetospheric lobes, these regions are  
174 not identical with the distant lobe; we therefore designate them as lobe-  
175 like regions. Yao et al. (2019) extracted lobe-like magnetic field  
176 ( $B_{lobe-like}$ ) values and demonstrated a clear correlation between  $B_{lobe-like}$   
177 variations and auroral morphology. Xu et al. (2023) further demonstrated  
178 that under quiet conditions,  $B_{lobe-like}$  values across different radial  
179 distances follow a fitting curve (the grey line in Figures 1(c) and 1(d))  
180 that is distinct from that observed during compressed times (blue line in

181 Figure 1(c)). The two curves reflect variations in the lobe-like magnetic  
182 field strengths and a global enhancement of magnetodisk current  
183 intensities under solar wind compression compared to the quiet period.  
184 These observed differences and variations suggest that  $B_{lobe-like}$  can serve as  
185 a reliable indicator of magnetospheric state. Furthermore, the lobe-like  
186 regions just outside the current sheet at low latitudes are particularly  
187 well-suited to capture the signature while minimizing confounding  
188 contributions from other current systems and the latitudinal variation of  
189 the planetary dipole field.

190 Specifically, we identified 10-hour intervals (approximately one Jovian  
191 rotation period) containing current sheet crossings. Within each interval,  
192 the lobe-like region was automatically selected by requiring the variance  
193 of magnetic field strengths within a sliding window to fall below the 10th  
194 percentile threshold computed across the entire interval. As shown in  
195 Figure 2(c), these selected regions consistently exhibit the expected  
196 characteristics: quasi-constant magnetic field and low plasma density. We  
197 then computed the average magnetic field strength over these selected  
198 lobe-like sub-intervals during each Jovian rotation period to obtain  
199 measured  $B_{lobe-like}$ . The distribution of  $B_{lobe-like}$  in Figure 2(d) exhibits a  
200 finite thickness. This spread reflects variations of  $B_{lobe-like}$  influenced by  
201 the intensity of the nearby disk currents. We compared the calculated  
202  $B_{lobe-like}$  values during the mission with the expected  $B_{lobe-like}$  values typical  
203 of a compressed or quiet magnetosphere to classify the magnetospheric  
204 states. As displayed in Appendix A, the two curves in Xu et al. (2023) can  
205 effectively classify events at 55–80  $R_J$  into distinct categories: events  
206 with  $B_{lobe-like}$  values near or above the upper curve are considered compressed  
207 events, while those near or below the lower curve are quiet events. At  
208 other locations, however, most events cluster within the same population  
209 and cannot be separated by the two curves, which is reasonable given that  
210 the model and dataset used in Xu et al. (2023) primarily focus on 55–80  $R_J$   
211 and lack constraints at other regions.

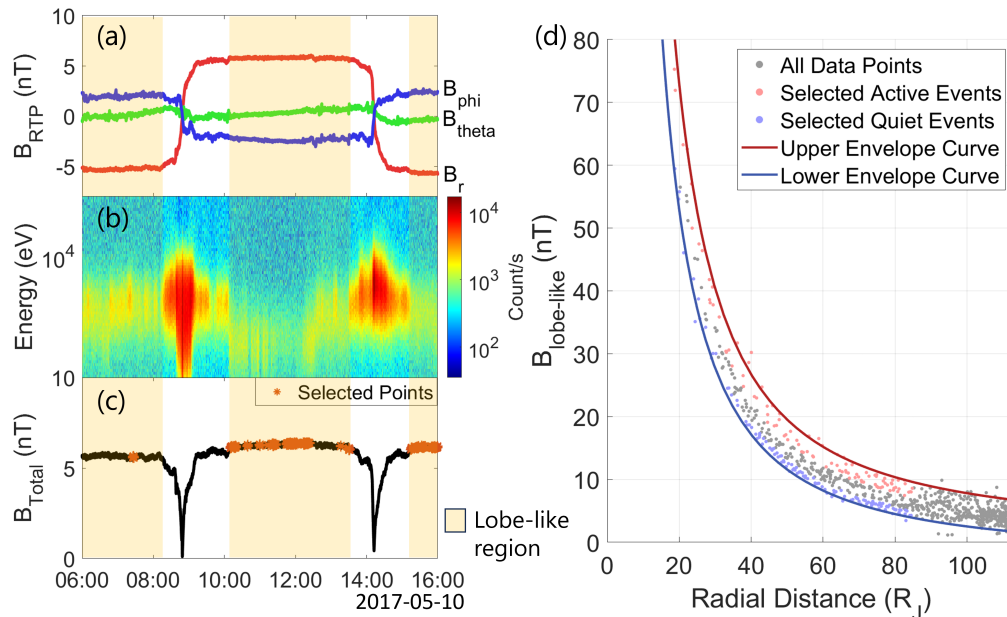
212 To better characterize  $B_{lobe-like}$  across different magnetospheric states and  
213 extend the method's applicability, we delineated the envelopes of  $B_{lobe-like}$ 's  
214 radial distribution. For the functional form of the envelopes, we adopt  
215 the expression:  $B_{lobe-like} = \sqrt{\vec{B}_{dipole}^2 + \vec{B}_{sheet}^2} = \sqrt{\frac{a}{r^6} + \frac{b}{r^n}} + c$ , where  $\frac{a}{r^6}$  originates from  
216 the characteristic  $r^{-3}$  decay of the planetary dipole field, while  $\frac{b}{r^n}$

217 represents contributions from current-induced magnetic fields. The  
 218 exponent  $n$  depends on the radial dependence of disk currents, and  
 219 coefficient  $b$  scales with the current intensity. Through fitting procedures  
 220 (detailed in Appendix A), we obtain upper and lower envelope curves with  
 221 the following analytical expressions:

$$222 \quad \text{Upper Curve: } B_{lobe-like} = \sqrt{\frac{1.167 \times 10^8}{r^6} + \frac{4.102 \times 10^7}{r^3}} + 1.408 \quad (1)$$

$$224 \quad \text{Lower Curve: } B_{lobe-like} = \sqrt{\frac{1.108 \times 10^8}{r^6} + \frac{2.454 \times 10^7}{r^3}} - 2.432 \quad (2)$$

225 The expressions for both upper and lower envelopes have similar  $a$  values,  
 226 in agreement with our theoretical expectation that the first term  
 227 primarily originates from the invariant intrinsic magnetic field  
 228 contribution. The identical exponent  $n=3$  indicates consistent radial  
 229 dependence of disk currents under different magnetospheric states. The  
 230 differing  $b$  values quantitatively demonstrate stronger current intensities  
 231 during compressed periods compared to quiet intervals, matching the  
 232 results reported in Xu et al. (2023). Collectively, these comparisons  
 233 support the overall reasonability of the fitting results.  
 234



235  
 236 **Figure 2.** Identification of magnetospheric states based on  $B_{lobe-like}$   
 237 measurements. (a-c) illustrate the lobe-like region selection process with  
 238 data from 10 May 2017. (a) R-Theta-Phi magnetic field components in

239 Jupiter-De-Spun-Sun (JSS) coordinates. (b) 100eV-100keV electron energy  
240 spectra measured by Jovian Auroral Distributions Experiment (JADE). (c)  
241 Total magnetic field strength. Orange stars denote points algorithmically  
242 selected as lobe-like using the criterion described in the main text. The  
243 orange shading indicates regions manually identified as lobe-like based on  
244 quasi-constant magnetic field and low plasma density. These points all lie  
245 within the orange-shaded regions, which demonstrates the reliability and  
246 effectiveness of our lobe-like region selection method. (d) Radial  
247 distribution of measured  $B_{lobe-like}$ . Red and blue curves indicate fitted upper  
248 and lower envelopes, respectively. Events are classified as compressed  
249 (light red; higher  $B_{lobe-like}$ ) or quiet (light blue; lower  $B_{lobe-like}$ ) based on  
250 these envelopes.

251  
252 The envelope curves enable systematic determination of magnetospheric  
253 states across extended radial distances as displayed in Figure 2(d). We  
254 classify the magnetosphere as quiet when  $B_{lobe-like} < B_{lower} + 0.2 \times B_{minus}$ , where  
255  $B_{lower}$  is the value given by the lower envelope curve and  $B_{minus}$  denotes the  
256 difference between the two curves; conversely, it is classified as a  
257 compressed state when  $B_{lobe-like} > B_{upper} - 0.45 \times B_{minus}$ , where  $B_{upper}$  is given by  
258 the upper envelope curve and the different coefficients are chosen because  
259 the data points near the upper envelope exhibit a sparser distribution  
260 compared to those near the lower envelope. We apply this criterion within  
261 15-85  $R_J$ . For regions inside 15  $R_J$ , the magnetic field is dominated by  
262 Jupiter's intrinsic field, with current-induced variations contributing  
263 little. Beyond 85  $R_J$ , the  $B_{lobe-like}$  values under the two states gradually  
264 converge as shown in Figures 1(c) and 1(d), making them nearly  
265 indistinguishable and introducing uncertainties. Through the criterion, we  
266 identify 118 quiet magnetospheric intervals and 99 compressed  
267 magnetospheric intervals (each event interval spans 10 hours, with a total  
268 of 414 qualified windows). The light red and blue points in Figure 2(d)  
269 mark our selected events respectively.

### 270 2.3. ULF Waves

271 ULF waves play a crucial role in energy transfer within the magnetosphere.  
272 Both theoretical models and studies on Earth have shown that ULF wave  
273 activity is closely associated with variations in interplanetary  
274 conditions and auroral emissions (Zong et al. 2017). In Jupiter's  
275 magnetosphere, Pan et al. (2021) demonstrated that ULF wave intensities

276 correlate significantly with the main aurora emissions and possibly also  
277 with polar emissions. Furthermore, Sun et al. (2024) established a  
278 correlation between quiet magnetospheric conditions and a low occurrence  
279 rate of 10-60 min ULF wave events, while these signals were observed  
280 across all time durations under compressed states identified according to  
281 auroral morphology. Figures 1(e) and 1(f) show the magnetic field  
282 fluctuations during compressed and quiet magnetospheric intervals,  
283 respectively. These results demonstrate that ULF wave activity in  
284 Jupiter's magnetosphere distinctly differs between compressed and quiet  
285 states under strong and weak solar wind conditions, suggesting ULF waves  
286 may serve as an effective proxy for determining magnetospheric states.  
287 State identification based on temporal variations of magnetospheric  
288 phenomena requires careful discrimination against artifacts introduced by  
289 the parameter's intrinsic spatial distribution and the spacecraft's  
290 changing position within the magnetosphere. Sun et al. (2024) identified  
291 significant latitudinal differences in ULF wave occurrence rates within  
292 Jupiter's magnetosphere, necessitating region-specific threshold  
293 adjustments. Here, our analysis primarily focuses on measurements in low-  
294 latitude regions exhibiting current sheet crossings within 10-hour windows  
295 for state classification, as these regions provide better ULF wave  
296 detectability. We performed wavelet analysis on 1-s resolution magnetic  
297 field data and integrated the power spectral density (PSD) across the 10-  
298 60 min period range over 10-hour windows. ULF wave energies in Jupiter's  
299 magnetosphere statistically vary with radial distance (Manners & Masters,  
300 2020). Accordingly, we binned the data by radial distance and identified  
301 events with wave intensities in the highest 25th percentile within each  
302 bin as compressed intervals, while those in the lowest 25th percentile  
303 were classified as quiet intervals. The same analytical processes were  
304 applied to both the total magnetic fields and the three background-  
305 subtracted magnetic field components in the mean field aligned (MFA)  
306 coordinate system, enabling us to examine the responses of compressional,  
307 transverse and overall wave activities. As shown in Appendix B, cross-  
308 validation revealed that fluctuations in all components potentially  
309 distinguish between magnetospheric states, with compressional waves  
310 demonstrating the best performance. This superiority likely stems from  
311 compressional waves' role as a more immediate conduit for solar wind  
312 energy input: external solar wind variations perturb the magnetopause,  
313 first launching fast-mode compressional waves that penetrate and undergo

314 transformation within the magnetosphere (Bentley et al. 2018). The  
315 correlation between compressional mode waves and X-ray flares reported in  
316 Yao et al. (2021) also suggests the crucial role of compressional waves in  
317 magnetospheric energy transport. Therefore, we selected compressional wave  
318 intensities as the diagnostic criterion, determining 213 intervals of  
319 quiet magnetospheric conditions and 213 intervals of compressed conditions  
320 (each event interval spans 10 hours, with a total of 881 qualified  
321 windows).

#### 322 2.4. Radio Emissions

323 Radio emissions offer a direct probe into particle acceleration sites and  
324 show potential as indicators of magnetospheric dynamics (e.g., Cecconi et  
325 al. 2022; Fogg et al. 2022). Jupiter's magnetosphere exhibits extensive  
326 radio emissions, among which broadband kilometric (bKOM) emissions are  
327 believed to be particularly sensitive to solar wind conditions (Zarka et  
328 al. 2021). Case studies by Louis et al. (2023) revealed that  
329 magnetospheric compressions could activate new radio sources, especially  
330 bKOM emissions. Chen et al. (2024) performed statistical analyses and  
331 demonstrated that during compressed states (identified based on  
332 magnetopause standoff distances measured during boundary crossings),  
333 Jovian bKOM emissions exhibited approximately 10-hour periodic occurrences  
334 with extended durations and broader frequency ranges. Conversely, in an  
335 expanded magnetosphere, bKOM emissions are typically absent, and the  
336 occasional observed emissions are also characterized by shorter durations  
337 and narrower frequency ranges. Figures 1(g) and 1(h) illustrate this  
338 comparison under compressed and quiet conditions, respectively.

339 To characterize the duration and frequency range of bKOM burst events  
340 comprehensively, we employed an area-based metric. This metric is defined  
341 as the total number of spectrogram grid points where the spectral density  
342 exceeded a predefined threshold (A) within the ~20-140 kHz frequency band  
343 (the LFR\_HI channels) in a 10-hour time window. In addition to metrics  
344 evaluated over one rotation period, persistent patterns, such as periodic  
345 enhancements or prolonged time durations of quiescence, could also provide  
346 critical constraints for identifying states of magnetospheric disturbance  
347 or stability. Our criteria specify that intervals are classified as quiet  
348 if the area remains below the quiet-state threshold (B) for more than  
349 seven consecutive rotation periods, and as compressed if the area exceeds  
350 an active-state threshold (C) for more than three consecutive rotation  
351 periods. This persistence-based criterion helps reduce false positives

352 associated with transient bursts or localized fluctuations. Considering  
353 the latitudinal dependence of bKOM emission occurrence rates reported by  
354 Louis et al. (2021), region-specific adjustments to the classification  
355 thresholds are necessary when analyzing measurements at different  
356 latitudes. The thresholds adopted in this study for Juno's low-latitude  
357 measurements with current sheet crossings during 10-hour windows were set  
358 as  $A = 5 \times 10^{-14} V^2/m^2/Hz$  for spectral density,  $B = 500$  grid points for the  
359 quiet state, and  $C = 3000$  grid points for the compressed state. We  
360 identified 237 quiet and 219 compressed intervals (each interval spans 10  
361 hours, with a total of 885 qualified windows).

### 362 3. RESULTS AND CROSS VALIDATION

363 We have summarized four methods for determining magnetospheric states:  
364 auroral morphologies,  $B_{lobe-like}$  values, ULF wave activities, and bKOM radio  
365 emissions. The lists of compressed and quiet intervals derived from each  
366 of these four methods are provided in Sun (2025). Among these potential  
367 proxies, auroral emissions offer global visibility of energy release  
368 processes, making them particularly valuable in characterizing large-scale  
369 magnetospheric responses. In this study, the aurora-derived classification  
370 dataset serves as a high-confidence benchmark against which we evaluate  
371 the reliability and applicability of the other three proxy methods. We  
372 systematically have examined whether the  $B_{lobe-like}$ , ULF wave, and radio  
373 emission methods could correctly identify the expected quiet or compressed  
374 states during Q-family and X-family auroral events, with the results  
375 summarized in Tables 1 and 2.

376 The analysis shows that both the  $B_{lobe-like}$  and ULF wave methods generally  
377 yield consistent results with auroral morphology identification, although  
378 several misclassifications occur possibly due to disturbances from local  
379 processes or temporal offsets between phenomena. For the results of radio  
380 emission identification, the quiet time list also shows acceptable  
381 consistency with Q-family auroral events. However, the performance in  
382 identifying compressed events is comparatively weaker. Four compression  
383 events in Table 2 were not successfully identified, three of which  
384 occurred during the early Juno orbits in 2016. Appendix C includes an  
385 illustration of Juno's orbits and the distributions of events that were  
386 correctly and incorrectly classified using the bKOM method. It can be seen  
387 that these misclassified events are mainly concentrated at large radial  
388 distances on the dawnside of Jupiter. The clustering of misidentified  
389

390 events may be not coincidental, and likely reflects a systematic bias  
391 introduced by the orbital effects.

392 In addition to the clustering of misclassified events in Tables 1 and 2,  
393 the overall distributions of the classification results also provide  
394 insight into the influence of orbital effects. During Juno's prime mission  
395 phase (2016–2021), the overall shape of its orbit remained essentially  
396 unchanged, but the apoapsis gradually precessed from the dawn sector  
397 through the nightside toward the dusk sector, while the orbital  
398 inclination steadily increased. Comparing the event lists from all four  
399 methods, we found that the auroral,  $B_{lobe-like}$  and ULF wave approaches  
400 provided relatively balanced distributions of quiet and compressed periods  
401 across different years. In contrast, the lists identified through radio  
402 emissions exhibit systematic biases: no quiet events are recorded after  
403 2019, and significantly fewer compressed events are identified in 2016  
404 compared to other methods. Our analysis has already been constrained to  
405 low-latitude regions, thereby excluding effects from latitudinal  
406 dependence. As previous studies have shown that bKOM emissions display  
407 almost uniform distributions with radial distance (Fischer et al. 2025),  
408 the influence of radial effects can therefore be ruled out. The observed  
409 imbalance may instead arise from local time variations caused by the orbit  
410 precession. Auroras and bKOM radio emissions both originate from the  
411 precipitation of charged particles along high-latitude magnetic field  
412 lines. Given that Jupiter's auroral brightness and morphology exhibit  
413 significant local time dependence (Groulard et al. 2024; Head et al.  
414 2024), it is plausible that bKOM radio emissions, which are associated  
415 with the same magnetospheric processes, may also display local time  
416 asymmetries similar to those observed in Jovian hectometric emissions and  
417 Saturn kilometric radiation (Boudouma et al. 2023; Lamy et al. 2009;  
418 Menietti et al. 1999; Zarka et al. 2021).

419 To explore potential improvements, an adjusted approach was tested: the  
420 bKOM data was normalised by local time binning, and events were then  
421 classified based on percentile rankings within each bin (events in the  
422 highest 25% were classified as compressed). The resulting list of  
423 compressed and quiet events was better balanced, comparable with other  
424 methods, and the agreement with auroral classifications was improved. This  
425 adjusted approach successfully identified most X-family auroral events,  
426 with the sole exception of Event 14. Nevertheless, we maintain a cautious

427 stance regarding the necessity of local time corrections, which requires  
 428 more comprehensive analyses of bKOM emissions' distribution.  
 429 Our comparative analysis demonstrates that  $B_{lobe-like}$  and ULF wave activities  
 430 can effectively reproduce magnetospheric state classifications derived  
 431 from auroral morphologies following appropriate spatial normalization. The  
 432 bKOM radio emissions also provide an acceptable indicator with additional  
 433 analysis and further correction. Collectively, these single-point  
 434 measurements affirm their effectiveness as proxies of magnetospheric  
 435 states. Moreover, we propose that combining multiple datasets can further  
 436 enhance identification reliability by providing a more comprehensive  
 437 assessment of magnetospheric states. Consistent results across different  
 438 methods would significantly mitigate the interference from local  
 439 processes, thereby reducing the probability of misclassification. Here, we  
 440 focus on the overlapping valid application ranges of the three methods,  
 441 the low-latitude region between 15–85  $R_J$ , to obtain their consensus  
 442 classifications. When a time window is concurrently identified as a quiet  
 443 or compressed event by at least two in situ measurement methods, it is  
 444 classified accordingly in the consolidated results. From a total of 414  
 445 qualified time windows, we identify 124 quiet and 113 compressed events  
 446 (Sun 2025). Notably, each in situ method independently identified ~25% of  
 447 events as quiet and ~25% as compressed, while the resulting consolidated  
 448 classifications also show similar proportions (~30% quiet, ~27%  
 449 compressed). The significant retention rates signify substantial overlap  
 450 in the event sets detected by the individual techniques and demonstrate  
 451 good consistency and robustness across the different methods. The  
 452 consolidated time lists complement the auroral morphology-based  
 453 classifications and enable more systematic and universal investigations of  
 454 solar wind-magnetosphere interactions.

455  
 456 **Table 1**

457 Determination of magnetospheric states during Q-family aurora intervals  
 458 using single-point measurement methods.

Index	Q-family Aurora Event Time (UT)	$B_{lobe-like}$	ULF waves	BKOM Radio Emissions
1	2016 Dec 4 12:44:51	×	√	×
2	2016 Dec 12 14:40:35	/	/	/

3	2016 Dec 12 16:15:22	/	/	/
4	2016 Dec 13 11:21:37	/	/	/
5	2016 Dec 15 07:50:44	/	/	/
6	2017 May 10 05:54:33	√	√	√
7	2017 May 10 10:40:39	√	√	√
8	2017 May 13 08:36:44	√	√	√
9	2017 May 15 11:28:13	√	√	√
10	2017 Jul 5 08:05:37	√	√	√
11	2017 Jul 6 23:49:38	√	√	√
12	2017 Jul 8 04:28:27	√	√	√
13	2017 Jul 8 06:01:24	√	√	√
14	2019 Mar 9 11:10:16	/	/	/
15	2019 Mar 28 20:50:57	/	/	/
16	2019 Apr 6 14:36:00	/	/	/
17	2019 Sep 7 09:48:50	/	/	/
18	2019 Sep 10 07:42:46	×	×	×
19	2019 Sep 13 13:33:29	/	/	/

459 **Note.** The time list provides the corresponding time at Juno corrected for  
460 light travel time at the start of the HST exposure from Grodent et al.  
461 (2018) and Palmaerts et al. (2024). Symbols are defined as: √ indicates  
462 successful identification of the target state (consistent with auroral-  
463 morphology based classification), × denotes failure to identify the target  
464 state, and / represents that the measurement position falls outside the

465 method's applicable range. Here, the target state refers to the quiet  
 466 state.

467  
 468 **Table 2**

469 Determination of magnetospheric states during X-family aurora intervals  
 470 using single-point measurement methods

Index	X-family Aurora Time (UT)	$B_{lobe-like}$	ULF waves	BKOM Radio Emissions
1	2016 Nov 30 14:57:23	/	√	×
2	2016 Nov 30 16:32:45	/	√	×
3	2016 Dec 1 16:23:32	×	√	×
4	2016 Dec 5 18:56:58	√	√	√
5	2016 Dec 6 14:02:21	√	√	√
6	2016 Dec 11 18:29:20	/	/	/
7	2017 Mar 17 08:01:34	√	√	×
8	2017 Mar 18 14:14:38	√	×	√
9	2017 Mar 19 09:19:18	√	√	√
10	2017 Jun 18 09:13:00	/	/	/
11	2019 May 22 21:24:30	√	√	√
12	2019 May 23 16:28:33	×	×	√
13	2019 Jul 20 13:15:38	/	/	/
14	2019 Sep 10 04:32:07	×	√	√

471 **Note.** The time list source and symbol definitions follow Table 1. Here,  
 472 the target state refers to the compressed state.

473  
 474

#### 4. DISCUSSION AND SUMMARY

475 Jupiter's magnetosphere displays a spectrum of states in response to  
476 varying solar wind conditions. In the continuum, this study focuses on  
477 characterizing and distinguishing two archetypal states representing  
478 opposite extremes: the quiet and compressed magnetosphere. We observe  
479 enhanced auroral emissions, elevated lobe magnetic fields, increased ULF  
480 wave activities, and more active (albeit comparatively less reliable) bKOM  
481 radio emissions in the compressed magnetosphere compared to the quiet  
482 magnetosphere. These indicators allow us to determine magnetospheric  
483 states even in the absence of in situ solar wind measurements. While  
484 auroral imaging provides global visibility, using single-point in situ  
485 measurements to infer the global state of Jupiter's complex magnetosphere  
486 requires careful consideration of several factors. First, temporal  
487 averaging over full Jovian rotations (~10 hours) is applied to  
488 comprehensively capture characteristic structures and processes across  
489 different rotational phases. Additionally, the inherent distributions of  
490 the indicators and their responses to external solar wind  
491 variations exhibit spatial variability across Jupiter's vast  
492 magnetosphere, necessitating normalization corrections or region-specific  
493 standards for accurate determination.

494 By addressing these considerations, our classification results derived  
495 from Juno-era data are deemed effective and reliable as confirmed by  
496 cross-validation. Consequently, these three in situ methods enable  
497 continuous monitoring of magnetospheric states and corresponding external  
498 conditions throughout most of the spacecraft's measurement period – far  
499 exceeding the temporal coverage of remote sensing and in situ solar wind  
500 measurements. The methodology and criteria are also applicable to past  
501 missions (e.g., Galileo) and future Jupiter exploration  
502 programs, following appropriate adaptations to account for instrumental  
503 and orbital differences.

504 Although the use of in situ observations provides valuable diagnostics,  
505 such methods also have limitations, since the response of magnetospheric  
506 phenomena does not occur instantaneously with changes in solar wind  
507 conditions. For example, in event #18 of Table 1, none of the three in  
508 situ proxies yielded a state determination consistent with the auroral  
509 method. We noticed that approximately three hours before event #18, the  
510 auroral morphology still exhibited X-family features (corresponding to  
511 event #14 in Table 2), suggesting that a transition in the magnetospheric  
512 state occurred within that three-hour interval. It is likely that

513 Jupiter's magnetosphere underwent a brief compression, with event #14  
514 capturing the final stage of the associated auroral response. Three hours  
515 later, although the auroral signatures had faded, some other responses in  
516 the system remained in a transitional phase, retaining residual effects of  
517 the prior compression. Notably, Juno was located near  $30 R_J$  at that time, a  
518 relatively inner region where the response to external conditions tends to  
519 exhibit a longer delay. The presence of response delays limits the ability  
520 of these observational methods to unambiguously identify the  
521 magnetospheric states. Different magnetospheric phenomena respond to  
522 external perturbations on distinct timescales, and even the same parameter  
523 may exhibit spatially dependent delays, all of which can naturally lead to  
524 occasional misclassifications. In future work, as the generation  
525 mechanisms of auroras, *B<sub>lobe-like</sub>* signatures, ULF waves, and bKOM emissions  
526 become better understood, their respective response times to solar wind  
527 perturbations will be further quantified. This progress will help further  
528 refine the use of these observables as reliable proxies for solar wind  
529 conditions.

530 In summary, both auroral remote sensing and the three in situ methods  
531 presented here facilitate temporally precise state determinations,  
532 creating opportunities for statistical time-series analyses that can  
533 advance our understanding of planetary magnetospheric response dynamics  
534 under varying solar wind conditions. Furthermore, this framework – though  
535 developed for Jupiter – could potentially be transferred to other  
536 planetary magnetospheres (e.g., Saturn, Uranus, Neptune), pending  
537 validation with respective mission data in the future.

538

## 539 5. ACKNOWLEDGEMENTS

540 All Juno data used here are publicly available from NASA's Planetary Data  
541 System (<https://pds-ppi.igpp.ucla.edu/>), including the MAG (Connerney  
542 2024), JADE (Allegrini et al. 2024), and WAVES (Kurth & Piker 2024)  
543 dataset.

544 ZY acknowledges the General Program of the National Natural Science  
545 Foundation of China (Grant 42374212) and the Research Grants Council (RGC)  
546 General Research Fund (Grant No. 17309124). YX was supported by the China  
547 Postdoctoral Science Foundation under Grant Number 2025M770390, and the  
548 Postdoctoral Fellowship Program of CPSF under Grant Number GZB20250099.  
549 L.C.R. was supported by STFC Grant ST/Y002148/1 to Lancaster University.

550 Project Supported by the Specialized Research Fund for State Key  
551 Laboratory of Solar Activity and Space Weather.

552

553

## APPENDIX

554

555

### A. DETAILS IN THE $B_{lobe-like}$ METHOD

556

557

558

559

560

561

In Figure 3(a), we compare the overall distribution of  $B_{lobe-like}$  values with the two curves representing compressed and quiet magnetospheric states as described in Xu et al. (2023). These two curves can effectively classify events at 55-80  $R_J$  into distinct categories. At other locations, however, most events cluster within the same population and cannot be separated by the two curves.

562

563

564

565

566

To fit the upper and lower envelopes, we first identify the boundary points showing the range of  $B_{lobe-like}$  variations at different radial distances. The data points are divided into 40 equally spaced bins, from which we select the largest and the smallest  $B_{lobe-like}$  values in each bin, as plotted in Figure 3(b).

567

Adopting the functional form,  $B_{lobe-like} = \sqrt{\vec{B}_{dipole}^2 + \vec{B}_{sheet}^2} = \sqrt{\frac{a}{r^6} + \frac{b}{r^n}} + c$ , we tested integer  $n$  values ranging from 1 to 6 to fit other parameters using the boundary points. Both envelopes achieved optimal fitting performance at  $n=3$ . Through nonlinear least-squares fitting, we obtained the following results:

568

569

570

571

572

$$Upper Curve: B_{lobe-like} = \sqrt{\frac{1.167 \times 10^8}{r^6} + \frac{4.102 \times 10^7}{r^3}} + 1.408, R^2 = 0.993 \quad (A1)$$

573

574

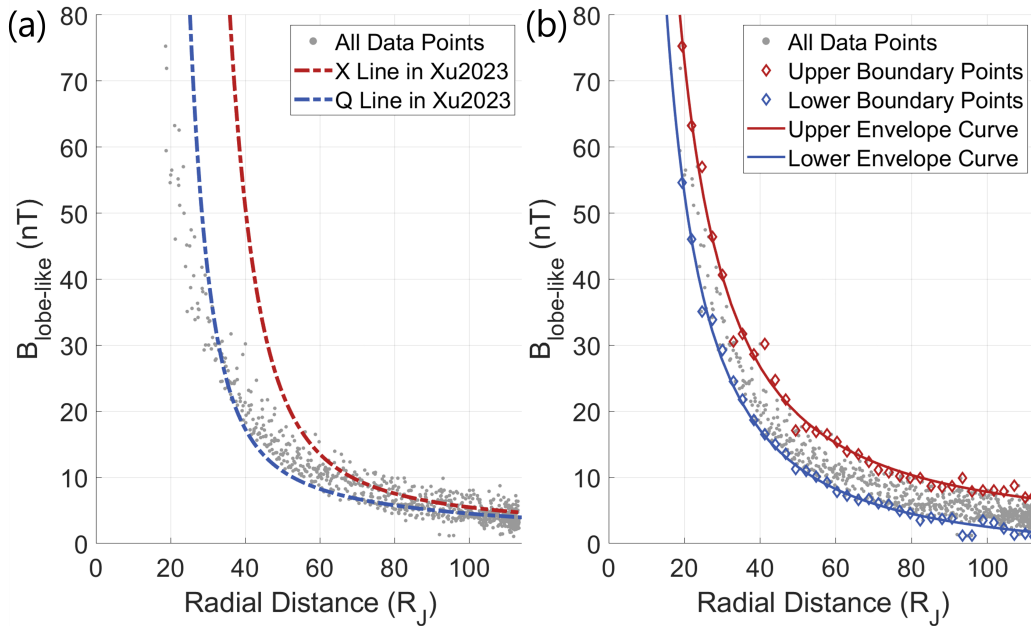
$$Lower Curve: B_{lobe-like} = \sqrt{\frac{1.108 \times 10^8}{r^6} + \frac{2.454 \times 10^7}{r^3}} - 2.432, R^2 = 0.995 \quad (A2)$$

575

576

577

The two fitted envelope curves and their performances are displayed in Figure 3(b).



578  
579 **Figure 3.** Distribution of  $B_{lobe-like}$  values across radial distances with  
580 trend-describing curves. (a) Gray points represent  $B_{lobe-like}$  values versus  
581 radial distance measured by Juno from July 2016 to July 2023, identical to  
582 the gray points in (b). The two lines are curves provided by Xu et al.  
583 (2023) describing  $B_{lobe-like}$  variations under different states. During quiet  
584 auroras,  $B_{lobe-like}$  values at different radial distances follow the Q line,  
585 distinct from those observed during X-family auroras (following X line).  
586 (b) Red diamonds mark the upper boundary points of  $B_{lobe-like}$  distribution,  
587 while blue diamonds indicate the lower boundary points. The red line  
588 represents the upper envelope curve fitted using upper boundary points,  
589 and the blue line shows the lower envelope derived from lower boundary  
590 points.

#### 591 B. DETAILS IN THE ULF WAVE METHOD

592 The Magnetic Field-Aligned (MFA) coordinate system employed in this work  
593 follows the definition:  $\vec{z} = \vec{b}$  (unit vector of the background magnetic field,  
594 computed via sliding averaging),  $\vec{y} = \vec{z} \times \vec{r}$  (where  $\vec{r}$  is the spacecraft  
595 position unit vector), and  $\vec{x} = \vec{y} \times \vec{z}$ . Wavelet analysis was applied to both  
596 the total magnetic field strengths and the background-subtracted magnetic  
597 field components in the MFA coordinate system to characterize ULF wave  
598 activities in Jupiter's magnetosphere, including compressional waves,  
599 transverse waves, and overall wave activities.

600 To compare the responses of magnetic field fluctuations across different  
601 components to external compression, we present the magnetospheric state

602 determination results based on wave intensities of different modes during  
603 Q/X-family aurora events in Tables 3 and 4. The diagnostic reliability  
604 increases with higher consistency between the classification results and  
605 those obtained from auroral morphology analysis. This cross-validation  
606 approach aligns with the methodology described in the RESULTS AND CROSS  
607 VALIDATION section of the main text. Based on the comparisons, we find  
608 that using the component parallel to the background magnetic field  
609 direction for wave analysis provides the most effective identification of  
610 magnetospheric states here.

611

612 **Table 3**

613 Determination of magnetospheric states during Q-family aurora intervals  
614 based on wave analysis using different magnetic field components.

Index	Q-family Aurora Time (UT)	$B_{\parallel}(B_z)$	$B_{\perp 1}(B_x)$	$B_{\perp 2}(B_y)$	$B_{total}$
1	2016 Dec 4 12:44:51	√	√	√	×
2	2016 Dec 12 14:40:35	/	/	/	/
3	2016 Dec 12 16:15:22	/	/	/	/
4	2016 Dec 13 11:21:37	/	/	/	/
5	2016 Dec 15 07:50:44	/	/	/	/
6	2017 May 10 05:54:33	√	√	√	√
7	2017 May 10 10:40:39	√	√	√	√
8	2017 May 13 08:36:44	√	√	√	√
9	2017 May 15 11:28:13	√	√	√	×
10	2017 Jul 5 08:05:37	√	√	√	√
11	2017 Jul 6 23:49:38	√	√	√	×
12	2017 Jul 8 04:28:27	√	√	√	√

13	2017 Jul 8 06:01:24	√	√	√	√
14	2019 Mar 9 11:10:16	/	/	/	/
15	2019 Mar 28 20:50:57	/	/	/	/
16	2019 Apr 6 14:36:00	/	/	/	/
17	2019 Sep 7 09:48:50	/	/	/	/
18	2019 Sep 10 07:42:46	×	×	×	×
19	2019 Sep 13 13:33:29	/	/	/	/

615 **Note.** The time list source and symbol definitions follow Table 1. Here,  
616 the target state refers to the quiet state.

617

618 **Table 4**

619 Determination of magnetospheric states during X-family aurora intervals  
620 based on wave analysis using different magnetic field components.

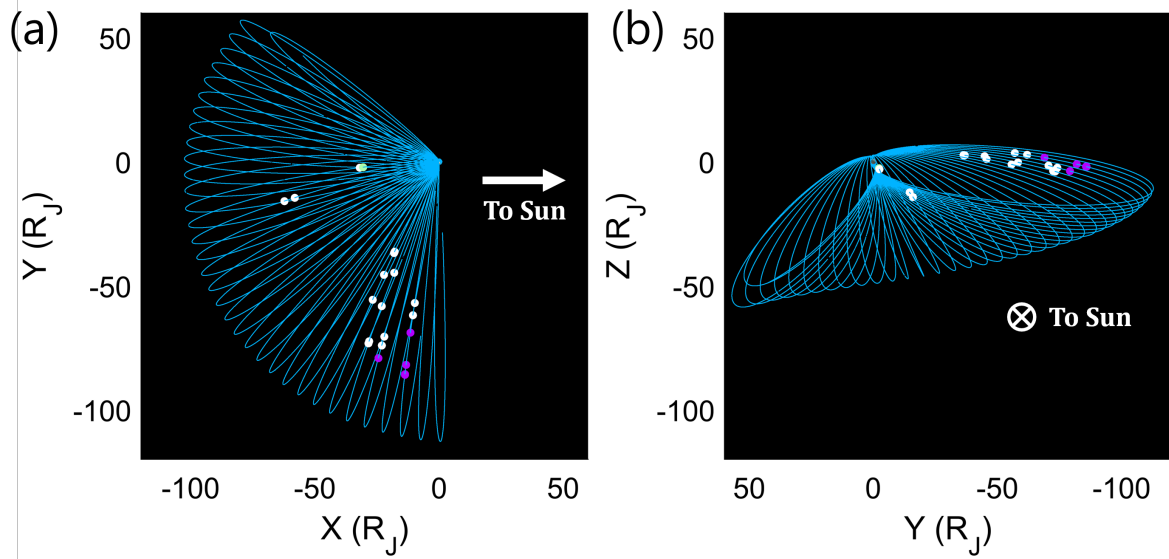
Index	X-family Aurora Time (UT)	$B_{\parallel}(B_z)$	$B_{\perp 1}(B_x)$	$B_{\perp 2}(B_y)$	$B_{total}$
1	2016 Nov 30 14:57:23	√	×	×	×
2	2016 Nov 30 16:32:45	√	×	×	×
3	2016 Dec 1 16:23:32	√	√	√	√
4	2016 Dec 5 18:56:58	√	√	√	√
5	2016 Dec 6 14:02:21	√	√	√	√
6	2016 Dec 11 18:29:20	/	/	/	/
7	2017 Mar 17 08:01:34	√	√	√	√
8	2017 Mar 18 14:14:38	×	×	×	√

9	2017 Mar 19 09:19:18	√	√	√	√
10	2017 Jun 18 09:13:00	/	/	/	/
11	2019 May 22 21:24:30	√	×	√	×
12	2019 May 23 16:28:33	×	×	×	×
13	2019 Jul 20 13:15:38	/	/	/	/
14	2019 Sep 10 04:32:07	√	√	√	×

621 **Note.** The time list source and symbol definitions follow Table 1. Here,  
622 the target state refers to the compressed state.

#### 623 C. DETAILS IN THE BKOM EMISSIONS METHOD

624 Figure 4 shows Juno's trajectory in the XY and YZ planes of the JSO  
625 coordinate system during its prime mission phase from July 2016 to August  
626 2021. In the JSO system, the X-axis points from Jupiter toward the Sun,  
627 the Z-axis is directed northward, normal to Jupiter's orbital plane around  
628 the Sun, and the Y-axis completes a right-handed Cartesian triad. Juno is  
629 a polar orbiter around Jupiter, with its orbital plane precessing  
630 gradually from the dawn sector through the nightside toward the dusk  
631 sector, accompanied by an increasing orbital inclination. White dots  
632 display Juno's locations of events where the magnetospheric states  
633 determined from auroral and bKOM observations are consistent (listed in  
634 Tables 1 and 2), whereas purple dots denote events where the two methods  
635 yield different results. Event #18 in Table 1 is marked in light green;  
636 for this event, none of the three in situ methods produced a result  
637 consistent with the auroral classification. This discrepancy likely arises  
638 from factors other than the limitations of the bKOM method and is  
639 therefore not discussed further here. It can be seen that the  
640 misclassified events in Tables 1 and 2, corresponding to both quiet and  
641 compressed states, are mainly concentrated along Juno's early orbits,  
642 i.e., at large radial distances on the dawnside of Jupiter.



643  
 644  
 645  
 646  
 647  
 648  
 649  
 650

Figure 4. Juno's trajectory in the (a) XY and (b) YZ planes of the JSO coordinate system, where X points from Jupiter toward the Sun and Z is northward normal to Jupiter's orbital plane. White dots mark Juno's positions of events with consistent magnetospheric-state identifications between auroral and bKOM methods, purple dots indicate inconsistent cases, and event #18 in Table 1 (light green) is excluded from discussion.

651 References

- 652 Allegrini, F., Wilson, R.J., Ebert, R.W., Loeffler, C. 2024, JUNO J/SW  
653 JOVIAN AURORAL DISTRIBUTION CALIBRATED V1.0, JNO-J/SW-JAD-3-CALIBRATED-  
654 V1.0, NASA Planetary Data System, doi: 10.17189/1519715
- 655 Bagenal, F. 2007, The magnetosphere of Jupiter: Coupling the equator to  
656 the poles, *JASTP*, 69(3), 387-402,  
657 <https://doi.org/10.1016/j.jastp.2006.08.012>
- 658 Bame, S. J., Barraclough, B. L., Feldman, W. C., et al. 1992, Jupiter's  
659 Magnetosphere: Plasma Description from the Ulysses Flyby, *Sci*, 257(5076),  
660 1539-1543, <https://doi.org/10.1126/science.257.5076.1539>
- 661 Barnard, L., & Owens, M. 2022, HUXt—An open source, computationally  
662 efficient reduced-physics solar wind model, written in Python, *FrP*, 10,  
663 1005621, <https://doi.org/10.3389/fphy.2022.1005621>
- 664 Bonfond, B., Yao, Z. H., Gladstone, G. R., et al. 2021, Are Dawn Storms  
665 Jupiter's Auroral Substorms? *AGUA*, 2(1), e2020AV000275,  
666 <https://doi.org/10.1029/2020AV000275>
- 667 Boudouma, A., Zarka, P., Magalhães, F. P., et al. 2023, Localisation of  
668 the main HOM source in the dusk side of the Jovian magnetosphere, 2023pre9  
669 conf, 103094, <https://doi.org/10.25546/103094>
- 670 Bridge, H. S., Belcher, J. W., Lazarus, A. J., et al. 1979a, Plasma  
671 Observations Near Jupiter: Initial Results from Voyager 1. *Sci*, 204(4396),  
672 987-991. <https://doi.org/10.1126/science.204.4396.987>
- 673 Bridge, H. S., Belcher, J. W., Lazarus, A. J., et al. 1979b, Plasma  
674 Observations Near Jupiter: Initial Results from Voyager 2, *Sci*, 206(4421),  
675 972-976, <https://doi.org/10.1126/science.206.4421.972>
- 676 Cecconi, B., Witasse, O., Jackman, C. M., Sánchez-Cano, B., & Mays, M. L.  
677 2022, Effect of an Interplanetary Coronal Mass Ejection on Saturn's Radio  
678 Emission, *FrASS*, 9, 800279, <https://doi.org/10.3389/fspas.2022.800279>
- 679 Chen, Y., Ye, S., Yao, Z., & Zhang, B. 2024, The Response of Broadband  
680 Kilometric Radiation to Compressions of the Jovian Magnetosphere, *ApJ*,  
681 972(2), 154, <https://doi.org/10.3847/1538-4357/ad6307>
- 682 Connerney, J. E. P., Benn, M., Bjarno, J. B., et al. 2017, The Juno  
683 Magnetic Field Investigation, *SSRv*, 213(1-4), 39-138,  
684 <https://doi.org/10.1007/s11214-017-0334-z>
- 685 Connerney, J. E. P. (GSFC) 2024, Juno MAG CALIBRATED DATA J V1.0, JNO-J-3-  
686 FGM-CAL-V1.0, NASA Planetary Data System, doi:10.17189/1519711
- 687 Ebert, R. W., Bagenal, F., McComas, D. J., & Fowler, C. M. 2014, A survey  
688 of solar wind conditions at 5 AU: A tool for interpreting solar wind-

689 magnetosphere interactions at Jupiter, *FrASS*, 1, 00004,  
690 <https://doi.org/10.3389/fspas.2014.00004>  
691 Fischer, G., Taubenschuss, U., Píša, D., Imai, M., & Kurth, W. S. 2025,  
692 Spectral Structures of Jovian Broadband Kilometric Radiation Revealed by  
693 Cassini and Juno, *JGRA*, 130(1), e2024JA032826,  
694 <https://doi.org/10.1029/2024JA032826>  
695 Fogg, A. R., Jackman, C. M., Waters, J. E., et al. 2022, Wind/WAVES  
696 Observations of Auroral Kilometric Radiation: Automated Burst Detection  
697 and Terrestrial Solar Wind - Magnetosphere Coupling Effects, *JGRA*, 127(5),  
698 e2021JA030209, <https://doi.org/10.1029/2021JA030209>  
699 Grodent, D., Bonfond, B., Yao, Z., et al. 2018, Jupiter's Aurora Observed  
700 With HST During Juno Orbits 3 to 7, *JGRA*, 123(5), 3299-3319,  
701 <https://doi.org/10.1002/2017JA025046>  
702 Groulard, A., Bonfond, B., Grodent, D., et al. 2024, Dawn-dusk asymmetry  
703 in the main auroral emissions at Jupiter observed with Juno-UVS, *Icar*,  
704 413, 116005, <https://doi.org/10.1016/j.icarus.2024.116005>  
705 Gurnett, D. A., Kurth, W. S., Hospodarsky, G. B., et al. 2002, Control of  
706 Jupiter's radio emission and aurorae by the solar wind, *Natur*, 415, 985,  
707 <https://doi.org/10.1038/415985a>  
708 Head, L. A., Grodent, D., Bonfond, B., et al. 2024, Effect of  
709 magnetospheric conditions on the morphology of Jupiter's UV main auroral  
710 emission as observed by Juno-UVS, *A&A*, 688, A205,  
711 <https://doi.org/10.1051/0004-6361/202450253>  
712 Head, L. A., Grodent, D., Bonfond, B., et al. 2025, Ultraviolet auroral  
713 bridge of Jupiter: The effect of the solar wind on the morphology of the  
714 polar aurora, *A&A*, 700, A142, <https://doi.org/10.1051/0004-6361/20255475>  
715 Jian, L. K., MacNeice, P. J., Taktakishvili, A., et al. 2015, Validation  
716 for solar wind prediction at Earth: Comparison of coronal and heliospheric  
717 models installed at the CCMC, *SpWea*, 13(5), 316-338,  
718 <https://doi.org/10.1002/2015SW001174>  
719 Keebler, T. B., Tóth, G., Zieger, B., & Opher, M. 2022, MSWIM2D: Two-  
720 dimensional Outer Heliosphere Solar Wind Modeling, *ApJS*, 260(2), 43,  
721 <https://doi.org/10.3847/1538-4365/ac67eb>  
722 Krupp, N., Woch, J., Lagg, A., et al. 2002, Leakage of energetic particles  
723 from Jupiter's dusk magnetosphere: Dual spacecraft observations, *GeoRL*,  
724 29(15), 26-1-26-4, <https://doi.org/10.1029/2001GL014290>

725 Krupp, N., Woch, J., Lagg, A., et al. 2004, Energetic particle  
726 observations in the vicinity of Jupiter: Cassini MIMI/LEMMS results, JGRA,  
727 109(A9), <https://doi.org/10.1029/2003JA010111>

728 Kurth, W. S., Gurnett, D. A., Hospodarsky, G. B., et al. 2002, The dusk  
729 flank of Jupiter's magnetosphere, *Natur*, 415(6875), 991-994,  
730 <https://doi.org/10.1038/415991a>

731 Kurth, W. S., Hospodarsky, G. B., Kirchner, D. L., et al. 2017, The Juno  
732 Waves Investigation, *SSRv*, 213(1), 347-392,  
733 <https://doi.org/10.1007/s11214-017-0396-y>

734 Kurth, W. S., & Piker, C. W. 2024, JUNO E/J/S/SS WAVES CALIBRATED SURVEY  
735 FULL RESOLUTION V2.0, JNO-E/J/SS-WAV-3-CDR-SRVFULL-V2.0, NASA Planetary  
736 Data System, doi: 10.17189/1520498

737 Lamy, L., Cecconi, B., Prangé, R., et al. 2009, An auroral oval at the  
738 footprint of Saturn's kilometric radio sources, colocated with the UV  
739 aurorae, JGRA, 114(A10), 10212, <https://doi.org/10.1029/2009JA014401>

740 Louis, C. K., Jackman, C. M., Hospodarsky, G., et al. 2023, Effect of a  
741 Magnetospheric Compression on Jovian Radio Emissions: In Situ Case Study  
742 Using Juno Data, JGRA, 128(9), <https://doi.org/10.1029/2022JA031155>

743 Manners, H., & Masters, A. 2020, The Global Distribution of Ultralow-  
744 Frequency Waves in Jupiter's Magnetosphere, JGRA, 125(10),  
745 <https://doi.org/10.1029/2020JA028345>

746 McComas, D. J., Szalay, J. R., Allegrini, F., et al. 2017, Plasma  
747 environment at the dawn flank of Jupiter's magnetosphere: Juno arrives at  
748 Jupiter, *GeoRL*, 44(10), 4432-4438, <https://doi.org/10.1002/2017GL072831>

749 Menietti, J. D., Gurnett, D. A., Kurth, W. S., & Groene, J. B. 1999, Local  
750 time dependence of Jovian radio emissions observed by Galileo, *GeoRL*,  
751 26(5), 569-572, <https://doi.org/10.1029/1999GL900047>

752 Nichols, J. D., Badman, S.V., Bagenal, F., et al. 2017, Response of  
753 Jupiter's auroras to conditions in the interplanetary medium as measured  
754 by the Hubble Space Telescope and Juno, *GeoRL*, 44(15), 7643-7652,  
755 <https://doi.org/10.1002/2017GL073029>

756 Nichols, J. D., Bunce, E. J., Clarke, J. T., et al. 2007, Response of  
757 Jupiter's UV auroras to interplanetary conditions as observed by the  
758 Hubble Space Telescope during the Cassini flyby campaign, JGRA, 112(A2),  
759 <https://doi.org/10.1029/2006JA012005>

760 Odstrcil, D. 2003, Modeling 3-D solar wind structure, *AdSpR*, 32(4), 497-  
761 506, [https://doi.org/10.1016/S0273-1177\(03\)00332-6](https://doi.org/10.1016/S0273-1177(03)00332-6)

762 Owens, M., Lang, M., Barnard, L., et al. 2020, A Computationally  
763 Efficient, Time-Dependent Model of the Solar Wind for Use as a Surrogate  
764 to Three-Dimensional Numerical Magnetohydrodynamic Simulations, *SoPh*,  
765 295(3), 43, <https://doi.org/10.1007/s11207-020-01605-3>

766 Palmaerts, B., Grodent, D., Bonfond, B., et al. 2024, Overview of a large  
767 observing campaign of Jupiter's aurora with the Hubble Space Telescope  
768 combined with Juno-UVS data, *Icar*, 408, 115815,  
769 <https://doi.org/10.1016/j.icarus.2023.115815>

770 Pan, D., Yao, Z., Manners, H., et al. 2021, Ultralow-Frequency Waves in  
771 Driving Jovian Aurorae Revealed by Observations From HST and Juno, *GeoRL*,  
772 48(5), <https://doi.org/10.1029/2020GL091579>

773 Reiss, M. A., Muglach, K., Mullinix, R., et al. 2023, Unifying the  
774 validation of ambient solar wind models, *AdSpR*, 72(12), 5275-5286,  
775 <https://doi.org/10.1016/j.asr.2022.05.026>

776 Russell, C. T. 2001, The dynamics of planetary magnetospheres, *P&SS*,  
777 49(10), 1005-1030, [https://doi.org/10.1016/S0032-0633\(01\)00017-4](https://doi.org/10.1016/S0032-0633(01)00017-4)

778 Rutala, M. J., Jackman, C. M., Owens, M. J., et al. 2024, A Multi-Model  
779 Ensemble System for the Outer Heliosphere (MMESH): Solar Wind Conditions  
780 Near Jupiter, *JGRA*, 129(6), e2024JA032613,  
781 <https://doi.org/10.1029/2024JA032613>

782 Smith, E. J., Fillius, R. W., & Wolfe, J. H. 1978, Compression of  
783 Jupiter's magnetosphere by the solar wind, *JGRA*, 83(A10), 4733-4742,  
784 <https://doi.org/10.1029/JA083iA10p04733>

785 Sun, J. 2025, The event list for "Determining the State of Jupiter's  
786 Magnetosphere Using In Situ and Remote Sensing Observations", Zenodo, doi:  
787 10.5281/zenodo.16355250

788 Sun, J. W., Xie, L., Yao, Z. H., et al. 2024, On the Global Features of  
789 the 10-60-Min ULF Waves in Jovian Magnetosphere: Juno Observations, *JGRE*,  
790 129(4), <https://doi.org/10.1029/2023JE008279>

791 Tao, C., Kataoka, R., Fukunishi, H., Takahashi, Y., & Yokoyama, T. 2005,  
792 Magnetic field variations in the Jovian magnetotail induced by solar wind  
793 dynamic pressure enhancements, *JGRA*, 110, A11208,  
794 <https://doi.org/10.1029/2004JA010959>

795 Xu, Y., Yao, Z. H., Zhang, B., et al. 2023, On the Relation Between  
796 Jupiter's Aurora and the Dawnside Current Sheet, *GeoRL*, 50(13),  
797 <https://doi.org/10.1029/2023GL104123>

798 Yao, Z., Dunn, W. R., Woodfield, E. E., et al. 2021, Revealing the source  
799 of Jupiter's x-ray auroral flares, *SciA*, 7(28),  
800 <https://doi.org/10.1126/sciadv.abf0851>

801 Yao, Z. H., Bonfond, B., Grodent, D., et al. 2022, On the Relation Between  
802 Auroral Morphologies and Compression Conditions of Jupiter's Magnetopause:  
803 Observations From Juno and the Hubble Space Telescope, *JGRA*, 127(10),  
804 <https://doi.org/10.1029/2021JA029894>

805 Yao, Z. H., Grodent, D., Kurth, W. S., et al. 2019, On the Relation  
806 Between Jovian Aurorae and the Loading/Unloading of the Magnetic Flux:  
807 Simultaneous Measurements From Juno, Hubble Space Telescope, and Hisaki,  
808 *GeoRL*, 46(21), 11632-11641, <https://doi.org/10.1029/2019GL084201>

809 Zarka, P., Magalhães, F. P., Marques, M. S., et al. 2021, Jupiter's  
810 Auroral Radio Emissions Observed by Cassini: Rotational Versus Solar Wind  
811 Control, and Components Identification, *JGRA*, 126(10),  
812 <https://doi.org/10.1029/2021JA029780>

813 Zieger, B., & Hansen, K. C. 2008, Statistical validation of a solar wind  
814 propagation model from 1 to 10 AU, *JGRA*, 113(A8),  
815 <https://doi.org/10.1029/2008JA013046>

816 Zong, Q., Rankin, R., & Zhou, X. 2017, The interaction of ultra-low-  
817 frequency pc3-5 waves with charged particles in Earth's magnetosphere,  
818 *RvMPP*, 1(1), 10, <https://doi.org/10.1007/s41614-017-0011-4>  
819